HiSST: 2nd International Conference on High-Speed Vehicle Science Technology
11–15 September 2022, Bruges, Belgium

Surface Pressure Measurements on a Free-Flying Cone at Mach 7 using Pressure Sensitive Paint

Chris Wheeler[1], Andrew Hyslop[1], Joao Vieira[1], Laurent Le Page[1], Mark K. Quinn[2], Nafiz H. K. Chowdhury[1] and Luke J. Doherty[1]

Abstract

Experiments have been conducted for the first time to investigate the use of binary pressure sensitive paint (PSP) on a free-flying aerodynamic model in the Oxford High Density Tunnel at Mach 7. The model was a 7° half angle cone with a 1.25 mm nose radius and overall length of 250 mm. A binary PSP consisting of a RuDPP3 pressure luminophore and Fluorescein reference luminophore was applied to the model. The model movement and response of the paint were tracked throughout the flight using high-speed videography. The model also featured an on-board inertial measurement unit, thereby providing simultaneous measurement of the aerodynamic forces and surface pressure distribution. The measured surface pressure was compared with analytical and numerical predictions and found to be ≈3kPa higher than expected.

Keywords: *pressure sensitive paint, free-flight, aerodynamics, hypersonic*

Nomenclature

Latin
$A(T)$ – Stern Volmer constant (function of temperature)
$B(T)$ – Stern Volmer constant (function of temperature)
I – intensity
$\tilde{I}$ – intensity ratio
$\tilde{I}_c$ – calibration intensity ratio, Eq. (3)
K – calibration constant, Eq. (5)
L – length, m
M – Mach number
p – pressure, kPa
p_p – pitot pressure, kPa
Re_u – unit Reynolds number, 1/m
S_T – temperature sensitivity, %/°C
T – temperature, K or °C
u_x – axial velocity, m/s
x – axial distance, m

Subscript
0 – total (condition)
d – dark image / no illumination
$i = \{r, p\}$ – signal index
p – pressure signal
R – at reference condition (pressure and temperature)
r – reference signal
T – at given temperature

1. Introduction

The field of aerodynamics is fundamental to understanding the efficiency of flight for a given vehicle geometry. As a flight vehicle passes through a fluid medium, the aerodynamic forces and moments that act result from the integration of fluid pressure and shear force components acting over the vehicle surface. Knowledge of the net aerodynamic force and moment coefficients or the surface pressure

[1] *Oxford Thermofluids Institute, University of Oxford, Oxford, United Kingdom, Corresponding author email: luke.doherty@eng.ox.ac.uk*
[2] *Department of Mechanical, Aerospace & Civil Engineering, University of Manchester, Manchester, United Kingdom*

distribution over the vehicle provides the designer insight into the aerodynamic performance, stability and control. Full-scale flight experiments can provide this information but are expensive and are not used in the early design phase of any vehicle. As a consequence, initial data are increasingly obtained through computational methods. However, full nose-to-tail simulations remain challenging as phenomena such as boundary layer transition and separation can be difficult to predict numerically [1]. Therefore, high quality aerodynamic experiments are still required to provide validation to the simulations.

The measurement of aerodynamic phenomena in hypersonic ground test facilities are challenging due to the typically short test times (tens of milliseconds to milliseconds) that can be generated. For techniques such as sting-mounted force-balances, the flow duration is often insufficient for quasi-steady force equilibrium to be achieved between the model and supporting structure [2]. This leads to difficulties in extracting the aerodynamic forces from the vibrating model-supporting structure assembly. Although methods have been developed to overcome these difficulties [3, 4], it has been shown experimentally that the sting influences the flow field, altering the wake pressure field and resultant force magnitude [5, 6, 7].

Recently the free-flight force measurement technique has been shown to eliminate the impact of sting interference and vibrational effects of a rigid mount [2] in short-duration testing such as in shock tunnels and Ludwieg Tubes. A free-flight experiment is conducted as follows; the model is released via a drop mechanism into the tunnel, when the model reaches the centre of the core flow, the tunnel fires and the model is allowed to move unconstrained in 6 degrees of freedom. As the model is not rigidly held in position, non-intrusive measurements of phenomena are required. Forces have been successfully measured in free-flight in short duration facilities through optical tracking methods [5] and direct measurement of accelerations through the use of accelerometers and gyroscopes [8, 9].

As the measurement of forces via. the free-flight technique has become more established, there is an increasing requirement to simultaneously measure the surface pressures and temperatures. Often free-flight models are small relative to the facility nozzle and consequently have limited internal volume which constrains the use of on-board pressure sensors. In comparison, pressure sensitive paint (PSP) offers an attractive non-intrusive, high-quality method for obtaining surface pressure measurements. In combination with optical tracking methods, the use of PSP during a free-flight experiment would permit the full surface pressure distribution and aerodynamic forces to be measured simultaneously using the same experimental infrastructure.

The purpose of the current work was to investigate the feasibility of utilizing a cost-effective, binary-PSP on a free-flying model in the University of Oxford High Density Tunnel (HDT). The 7° half-angle free-flight cone model and infrastructure developed by Hyslop et al. [10] were used. A binary PSP mixture using RuDDP3 and Fluorescein luminophores was applied to the model which was tested in the HDT at a Mach 7 test condition with test time on the order of 50 ms.

The structure of the remainder of the paper is as follows – Section 2 describes the basic principles of operation of pressure sensitive paint and the results of a benchtop investigation of different mixture formulations. Section 3 then describes experimental set up including the wind tunnel, test condition, free-flight cone model and optical set up and data reduction techniques. Section 4 presents the results of both an in-situ calibration of the PSP coated cone model and a test at Mach 7 before some conclusions are drawn in Section 5.

2. Pressure Sensitive Paint

2.1. Principles of Operation

Pressure-sensitive paint (PSP) is an optical method of measuring static pressure over an entire surface non-intrusively using cameras. There are many variations of PSP in terms of chemical composition, surface application, and imaging; however, at the most basic level the technique works by measuring a change in intensity of emitted light due to the presence of atomic oxygen. The emitted light intensity is a function of both the local concentration atomic oxygen and illumination intensity. Single-component PSP is applied in this way by measuring the reduction in emitted light as oxygen concentration (and by Henrys' law, pressure) is increased. However, in order to make quantitative measurements of pressure, it is normally necessary to compare the signal measured to a known, static, reference condition. In this

Wheeler, C., Hyslop, A., Vieira, J., Le Page, L., Quinn, M., Chowdhury, N.H.K., Doherty, L.J.

experiment, as the model is moving through the test section and there is no guarantee of a uniform illumination field, a reference sensor is required to be included in the PSP formulation. PSP methodologies such as this, involving an oxygen-sensitive and an oxygen-insensitive luminescent compound are known as binary PSPs. These two signals need to be measured individually and ratioed using the well-known Stern Volmer equation given below where I refers to intensity, $\tilde{I}$ is an intensity ratio, p is pressure, A and B are calibration constants (which are usually a function of temperature, T), and subscript R refers to a reference condition.

$$\tilde{I} = \frac{I_R}{I} = A(T)\frac{p}{p_R} + B(T) \tag{1}$$

In this work the data was analysed using the so-called ratio-of-ratios –

$$\frac{\tilde{I}_R}{\tilde{I}} = \frac{I_{R,p}/I_{R,r}}{I_p/I_r} = \frac{A_p(T)\frac{p}{p_R} + B_p(T)}{A_r(T)\frac{p}{p_R} + B_r(T)} \tag{2}$$

where subscript *p* refers to the pressure signal and subscript *r* refers to the reference signal. The luminophore combination used in this study is RuDPP3 and fluorescein as the pressure and reference sensor respectively. Both of these compounds absorb light around 450 – 500 nm but exhibit different Stokes shifts meaning their output spectra are different as shown in Fig. 1. This property enables the two signals to be separated chromatically and measured using different optical filter combinations.

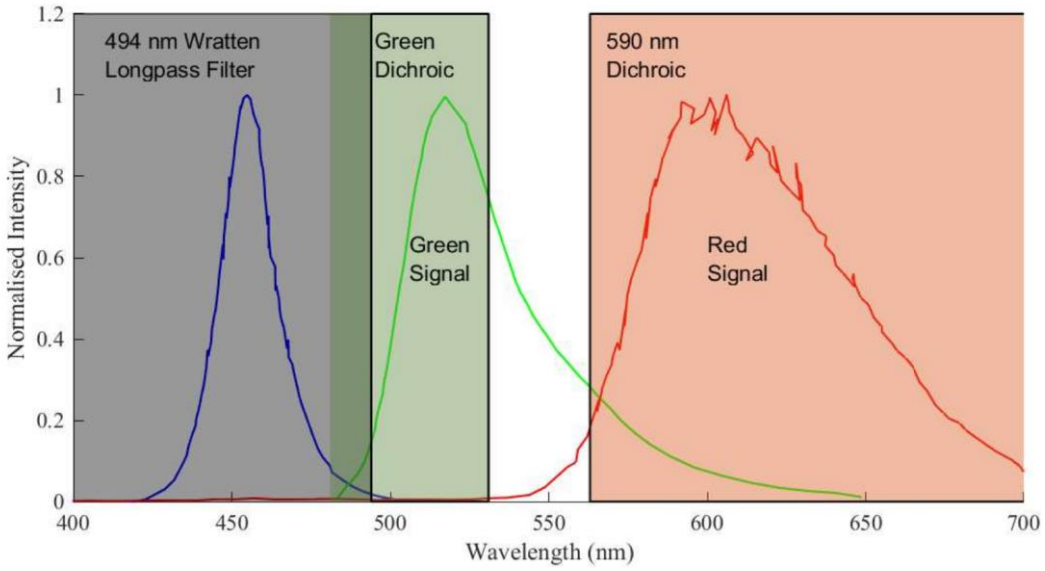

Fig. 1 PSP Spectrum showing illumination source (blue) [11], Fluorescein (green) [12] and RuDPP3 (red) [13] and the optical filters used to separate the signals.

The temporal response of PSP also needs to be considered for this study given the transient nature of the flow. The method of application of PSP to a surface is the primary determining factor in the coating's response time. Gregory et al. [14] and more recently Peng & Liu [15] showed various methods of applying PSP and preparing porous substrates, highlighting that a frequency response of several kHz is achievable with the correct preparation method. Anodized aluminum is a commonly used porous PSP substrate and has excellent temporal response; however, it is rather sensitive to temperature and is somewhat limited to simple geometries. A sprayable porous substrate, such as a polymer ceramic mixture, is the most common fast response PSP application method and, although it can be tricky to spray, is extremely versatile.

2.2. Benchtop Calibration Rig

The benchtop calibration rig developed by Vieira [16] was used to evaluate the pressure and temperature sensitivities of different mixtures of RuDPP3 and Fluorescein. The rig consisted of cylindrical pressure vessel with clear Perspex lid, light source and camera, housed within an opaque enclosure. The pressure vessel was 300 mm in diameter and 50 mm tall and could be evacuated using

an Edwards Vacuum E2M1.5 oil sealed rotary vane pump or pressurized using an Additel 914 hand operated pump. The pressure was measured using an Omega PXM219-002A10V transducer with a range 0 to 200 kPa absolute and accuracy ±1% of the reading. Each PSP mixture was deposited onto individual 75 mm square, 3 mm thick aluminium test coupons. Only a single test coupon could be calibrated at a time. Each coupon was mounted inside the pressure vessel onto an Adaptive Peltier cooler (P/N ET-127), thereby enabling the coupon temperature to be varied. The temperature of each coupon was independently measured using an RS Pro PT1000 RTD sensor with accuracy ±0.15 °C (Class A).

In this work, illumination was provided by a single Luminus Devices PT-120-B-L11-EPG LED which was powered at 2 amps. This is the same type of LED as used in the wind tunnel experiments. A Thorlabs MFF102 Filter Flipper was used to easily swap between the green bandpass dichroic filter (UQG Optics P/N CDG-5051) and a red long pass dichroic (Knight Optical P/N 590FDL) each mounted parallel to the coupon. Further discussion regarding the LED and selection of the filters is provided in Section 3.4. Images of the sample were recorded using a Bigeye G-283B Mono14 CCD camera fitted with a 75 mm Tamron lens.

For each coupon calibrations were completed over the range 0.5 kPa to 100 kPa and 20 to 40 °C. The typical calibration procedure was as follows: the pressure was set by operating the Edwards vacuum pump continuously and adjusting the leak rate into the pressure vessel. A Laird PID controller (P/N TC-XX-PR-59) was used to set the coupon sample. Once steady state was achieved, the light source was (manually) turned on and a Matlab code executed to record 20 images of the coupon through each optical filter. The temperature was subsequently altered to the next set point with the pressure only adjusted once all temperatures had been characterised. To facilitate calibrations at different pressures the coupon temperature was cycled.

2.3. Benchtop Calibration Data Reduction

For each calibration point, the recorded images were processed using the following steps:

1. The 20 images captured were averaged to give a single calibration image at each temperature and pressure, for both optical filters.
2. A single region of interest was chosen, and the intensity was spatially averaged to give I_i where $i=p$ for the RuDPP3 pressure signal (red filter) and $i=r$ for the reference Fluorescein signal (green filter). The region of interest was chosen such that is was not affected by the presence of the mounting screws or PT1000 RTD.
3. For each signal, a normalized intensity $\tilde{I}_c$ was calculated according to:

$$\tilde{I}_{c,i} = \frac{I_{R,i} - I_{d,i}}{I_i - I_{d,i}} \tag{3}$$

   where I_R is the average intensity measured at the reference condition and I_d is the average intensity recorded with no illumination.
4. Photodegradation correction: degradation of the PSP over the course of a calibration was accounted for by linearly interpolating between three calibration points at the reference conditions, recorded at the start, middle and end of a set of calibrations.
5. Calculate the ratio-of-ratios according to Eq. (2).

For the benchtop calibration, the reference condition for the calculation of I_R was taken to be 100 kPa and 20 °C. The subtraction of I_d in Eq. (3) acts to remove any effect of camera sensor noise on the results.

Table 1. Summary of Binary PSP mixtures evaluated in the calibration rig

Solution:		(1)			(2)			Luminophore Concentration			
No:	Type:	$RuDPP_3$ (X mg)	Fluorescein (Y mg)	DCM (ml)	RTV-118 (mg)	TiO_2 (g)	Toluene (ml)	Ru:F (1:x)	[Fluores] [mM]	[$RuDpp_3$] [mM]	[Ru + F] [mM]
a	PC-PSP	7.02	3.99	6	300	1.7	14	2	0.6	0.3	0.9
b	PC-PSP	4.68	2.66	6	300	1.7	14	2	0.4	0.2	0.6
c	PC-PSP	2.34	1.33	6	300	1.7	14	2	0.2	0.1	0.3
d	PC-PSP	14.03	3.99	6	300	1.7	14	1	0.6	0.6	1.2
e	PC-PSP	9.35	2.66	6	300	1.7	14	1	0.4	0.4	0.8
f	PC-PSP	4.68	1.33	6	300	1.7	14	1	0.2	0.2	0.4
g	PC-PSP	9.35	3.99	6	300	1.7	14	1.5	0.6	0.4	1
h	PC-PSP	6.24	2.66	6	300	1.7	14	1.5	0.4	0.27	0.67
i	PC-PSP	3.12	1.33	6	300	1.7	14	1.5	0.2	0.13	0.33
o	PC-PSP	9.35	0.00	6	300	1.7	14	N/A	0.0	0.4	0.4
p	PC-PSP	0.00	2.66	6	300	1.7	14	N/A	0.4	0.0	0.4
k	AA-PSP	14.03	3.99	20	N/A	N/A	N/A	1	0.6	0.6	1.2
l	AA-PSP	9.35	3.99	20	N/A	N/A	N/A	1.5	0.6	0.4	1.0
n	AA-PSP	14.03	2.66	20	N/A	N/A	N/A	2	0.4	0.2	0.6

2.4. Benchtop Calibration Results

A total of 14 different mixtures of RuDPP3 and Fluorescein were tested in the calibration rig as summarized in Table 1. The basic recipe on which these mixtures were based was that formulated by Egami et al. [17] (and also reported in Appendix C of [18]). As the experimental model to be used featured both aluminium and steel components (Section 3.3) both anodised aluminium PSP (AA-PSP) and polymer-ceramic PSP (PC-PSP) were investigated. There were nine core coupons of PC-PSP (labelled *a* – *i*), two single-component PC-PSP's (*o* & *p*) with just the pressure and reference luminophore respectively, and three AA-PSP's (*k*, *l* & *n*). Access to a dedicated anodization bath was limited in this work so efforts were primarily focused on PC-PSP. All coupons, except half of coupon *n*, used a white base-layer and each was sprayed with approximately 6 cross-coats.

Typical results achieved from the calibration rig are shown in Fig. 2 for coupon *b*. As expected, the RuDDP3 intensity (Fig. 2a) varies significantly over the entire calibration range and has a linear response over the pressure range of interest 1 to 10 kPa (absolute). Fig. 2a also shows a strong temperature dependency on the RuDDP3 intensity at a given pressure. In comparison, the Fluorescein luminosity results (Fig. 2b) show very little effect of temperature but do display a noticeable pressure dependency over the range 1 to 10 kPa. This pressure dependency was not expected and, from analysis of the single-component coupons *o* & *p*, was identified to due to RuDDP3 luminosity leaking through the green bandpass dichroic filter. This was rectified in later calibrations and the wind tunnel experiments by mounting the green dichroic filter at an angle of 45° relative to the light path, thereby reducing the pressure dependency of the Fluorescein reference signal to be less than 7%.

Three metrics were used to evaluate the different mixtures: (1) the mixture pressure sensitivity, that is, the gradient of the RuDPP3 response over the pressure range of interest (0 – 10 kPa abs.), (2) the temperature sensitivity of the mixture, and (3) robustness of the paint. The temperature sensitivity was calculated based on the 20°C and 30°C calibration results according to –

$$S_T = 100\left(\frac{I_T - I_{T,R}}{I_{T,R}}\right)/\Delta T \tag{4}$$

where S_T is the temperature sensitivity (in %/°C), I_T is the intensity at a given temperature (and constant pressure), $I_{T,R}$ is the intensity at the reference temperature, and ΔT is the difference in temperature.

Results for the pressure and temperature sensitivities are presented in Fig. 3 relative to the absolute calibration pressure. The temperature sensitivity was in the range 0.2 to 1 %/°C (depending on the formulation) which is consistent with literature [18], although there is some scatter for each mixture. This scatter is attributed to the small temperature range over which the sensitivity was calculated. Of those mixtures examined, solution *g* was chosen for use in the wind tunnel test campaign as it displayed a low temperature sensitivity, was relatively robust, and had good pressure sensitivity. The higher concentration of Fluorescein in solution *g* was also expected to improve the signal-to-noise ratio of the

reference luminosity in the wind tunnel experiments. Of the anodised aluminium solutions *k, l* and *n*, solution *n* was chosen for use in the wind tunnel testing for aluminium components of the model. The next section describes the experimental set up and wind tunnel, with Section 3.5 presenting the results of an in-situ PSP calibration.

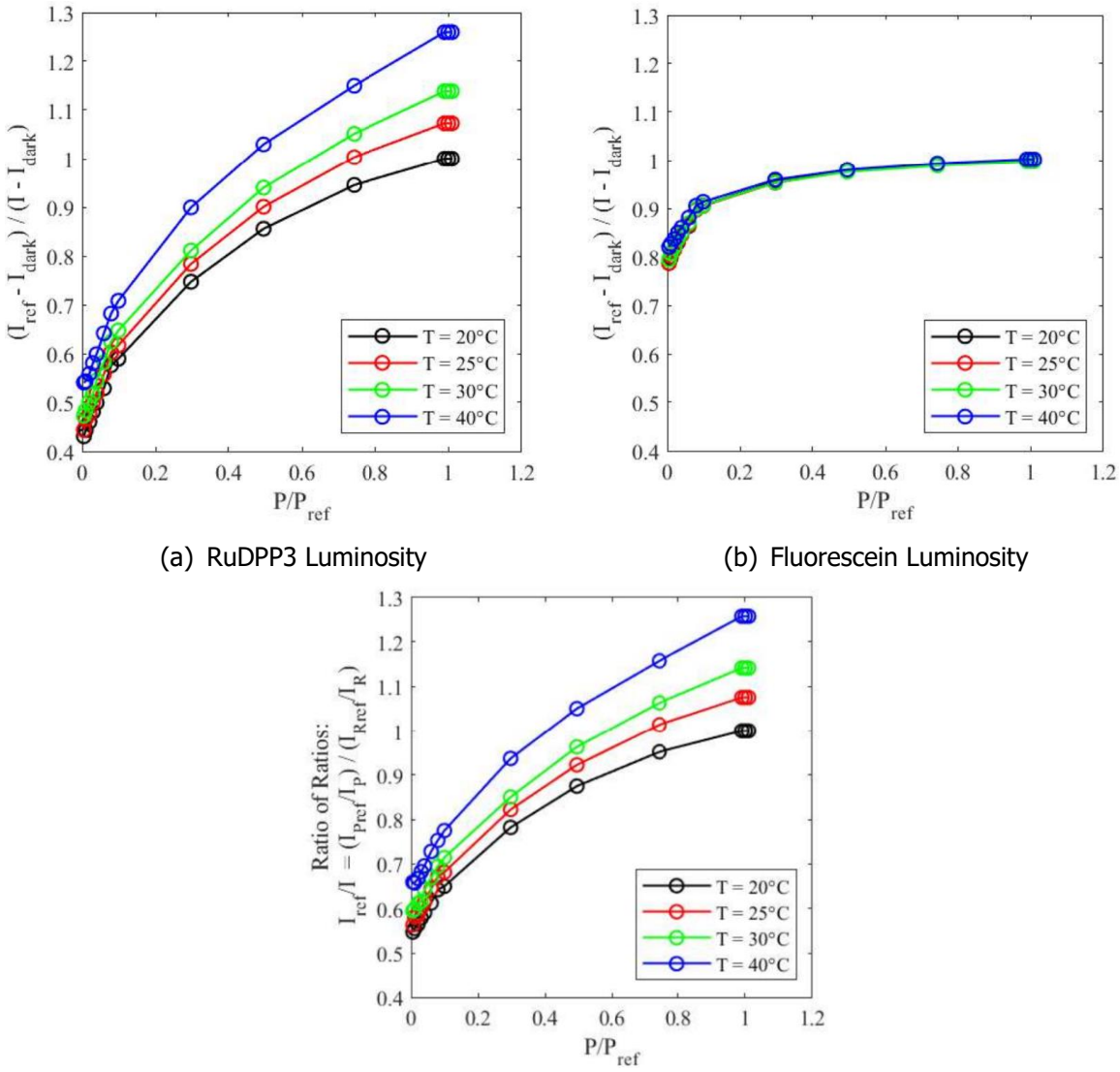

(a) RuDPP3 Luminosity

(b) Fluorescein Luminosity

(c) Ratio-of-ratios

Fig. 2 Sample calibration results for Coupon *b*. All intensities have been normalised and adjusted for photodegradation.

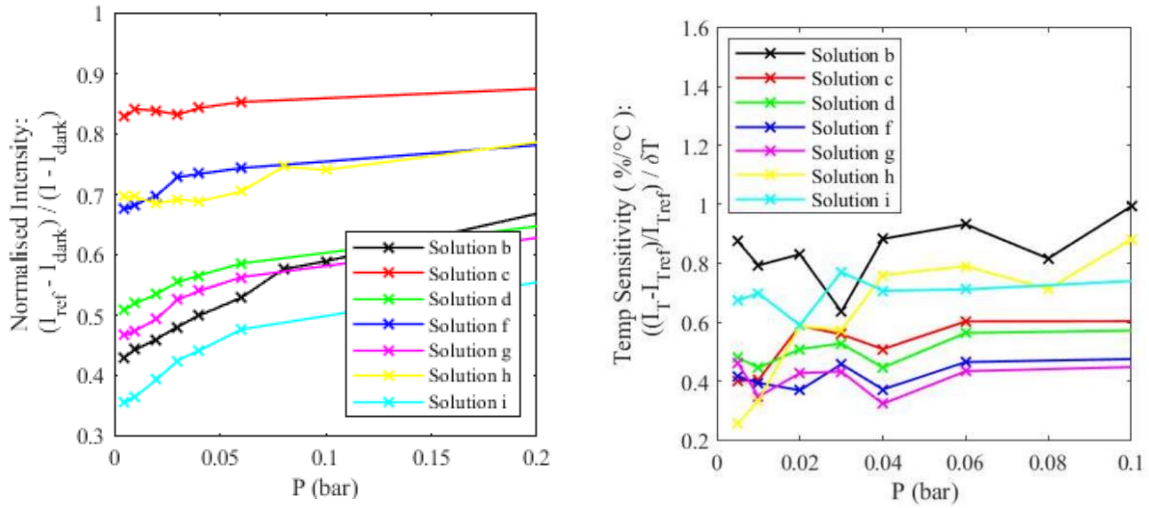

(a) Pressure signal sensitivity

(b) Temperature sensitivity calculated over the range 20 to 30°C

Fig. 3 Comparison of pressure and temperature sensitivity for different mixtures. The reference condition was taken to be 100 kPa and 20°C.

3. Experimental Setup

3.1. Oxford High Density Tunnel

Experiments to investigate the use of binary-PSP on a hypersonic free-flying model were conducted in the Oxford High Density Tunnel (HDT) located within the Oxford Thermofluids Institute. This facility is capable of generating relatively long duration flows at high Reynolds number, and is suitable for both steady and unsteady aerothermodynamic testing of hypersonic configurations. It features a 6-inch (152.4 mm) diameter barrel that is approximately 17.4 m in length. In this work the facility was operated as a heated Ludwieg Tube mode using a Mach 7 contoured nozzle with exit diameter 350 mm. Further details regarding the facility are presented in McGilvray et al. [19] and Wylie et al. [20].

3.2. Test Condition

The test flow properties were inferred from the measured nozzle supply pressure (p_0) and results from a prior nozzle survey which characterized the nozzle exit pitot-to-supply pressure ratio (p_p/p_0) and total temperature of the flow (T_0). Nozzle exit flow properties were calculated assuming isentropic flow of calorically perfect air with Keyes model used for the calculation of viscosity.

In both the current experiments and nozzle survey experiment the facility nozzle supply pressure was measured using a Kulite XCQ-080 absolute pressure transducer with a range of 0 to 7000 kPa and accuracy ±0.1% full scale (FS). For the nozzle survey, the pitot pressure was measured using a Kulite XCQ-093 absolute pressure transducer with a range of 0 to 689 kPa (100 psi) and accuracy ±0.1% FS and the total temperature was measured using an aspirated thermocouple probe. The probe design was based on the work of Widodo and Buttsworth [21] and Hermann et al. [22] and used a K-type thermocouple with nominal diameter 0.003 inch. The uncertainty in total temperature measurement with this probe was taken to be ±15 K [22].

The calculated test condition and corresponding uncertainty are given below in Table 2.

3.3. Experimental Model and On-board Data Acquisition System

The experimental model developed by Hyslop [10] was used for the current work. For completeness, a brief description is provided here. As shown in Fig. 4 the model is a 7° half angle cone with base diameter 63.6 mm and overall length of 250 mm. The model featured a removable aluminium nose piece with nose radii 1.25 mm. Steel hollow body halves allowed easy mounting of the on-board DAQ which was supported by a 3D printed holder. The model mass and centre-of-gravity (CoG) could be

adjusted using tungsten ballast. In this work the model mass was measured using a Sartorius ENTRIS 6231-1S precision scales to be 669.13 ± 0.01 g. The CoG location was measured to be 84.2 ± 0.1 mm upstream of the cone base using a moment balance, whereby the model was suspended via. two strings and the tension in the upstream string measured using an Applied Measurements Ltd Load Cell (P/N DPPSMM-1kg-002-000). This location corresponds to the theoretical centre-of-force location at 0° angle-of-attack (AoA). Consequently, the model exhibits minimal pitch during an experiment.

Table 2. Test Flow Condition

	Parameter	Units	Value	Uncertainty
Measured	p_0	kPa	3375	±7
Assumed	p_p/p_0	-	0.0149	±0.0002
	T_0	K	555	±15
Calculated Freestream	M	-	7.05	±0.02
	p	Pa	780	±16
	T	K	51	±1.4
	u_x	m/s	1006	±14
	Re_u	10^6/m	16.5	±0.8

Internal to the model was an on-board data acquisition system (DAQ) which contained a six degree-of-freedom inertial measurement unit (IMU) consisting of an integrated 3-axis accelerometer and 3-axis gyroscope, non-volatile memory, a Bluetooth radio module and a microcontroller. This DAQ was designed and built by the University of New South Wales Canberra and previously demonstrated capable of accurate measurement of acceleration and angular velocities in a hypersonic wind tunnel [23, 9]. The full-scale range of the accelerometer and gyroscope were ±16 g and ±2000 deg/s with maximum data rates 4 kHz and 8 kHz (respectively). Non-linearity of the accelerometer and gyroscope axis is reported to be 0.1% and 0.5% respectively. For this work a sample rate of 8 kHz was used which allowed for ~320 samples over the 40 ms duration of the experiment. Triggering of the instrument was achieved by detection of sustained free-fall upon model release.

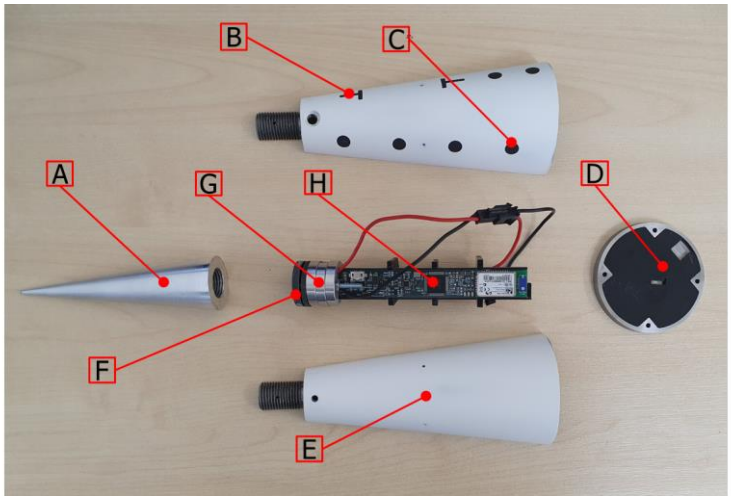

Fig. 4 Free-flight cone model (sans PSP). A – Aluminium nose; B – Electromagnetic alignment marker; C – Optical tracking dots; D – Steel rear with 3D printed insert; E – Steel cone half; F – 3D printed DAQ mount; G – Tungsten ballast; H – DAQ.

3.4. Optical Setup

A schematic of the optical setup is provided in Fig. 5. Internal to the test section, illumination was provided by six Luminus Devices PT-120-B-L11-EPG LEDs. These were chosen as their peak wavelength (460 nm) efficiently excites the luminophores, their small size provides freedom of mounting and their high angular distribution (giving nearly 50% power at 60° off-centreline) eased alignment constraints. The six LEDs were mounted using bespoke supports that consisted of a copper heat sink disk, a FATH24 pivot joint and aluminium baseplates that provided rotation adjustment. The LEDs and associated supports are seen clearly in Fig. 8. The LEDs were connected in series and powered using a Velleman laboratory power supply (P/N. LABPS3030SM) operated at 18 A (constant-current) via a bespoke interlock box. This setup was found to safely and effectively illuminate the entire flight path of the vehicle with sufficient intensity for the high-speed cameras.

External to the test section, three optical filters were used to split the pressure signal from the reference signal and remove reflected light from the illuminating LEDs. The filters used were as follows:

1) A 590 nm long-pass dichroic; dimensions 115 x 85 x 1.1 mm (Knight Optical P/N 590FDLxx) was used to perform the initial split of the pressure and reference/illumination signals.
2) A green bandpass dichroic; dimensions 100 x 100 x 1.1 mm (UQG Optics P/N CDG-1001) was mounted at 45° to the reference signal and used to remove any leakage of the pressure signal into the reference signal (as identified in the benchtop calibration results, see Section 2.4).
3) A 494 nm Wratten long-pass filter, dimensions 75 mm x 75 mm x 0.1 mm (Knight Optical P/N 494FWP7575), was used to remove the illumination source from the reference signal.

Fig. 1 shows the overall spectra expected to be received by each camera and the bandpass of each filter. One advantage of this optical set up and the use of a dichroic for filter #1 is that an identical optical path is maintained for imaging by both cameras, without sacrificing resolution or framerate.

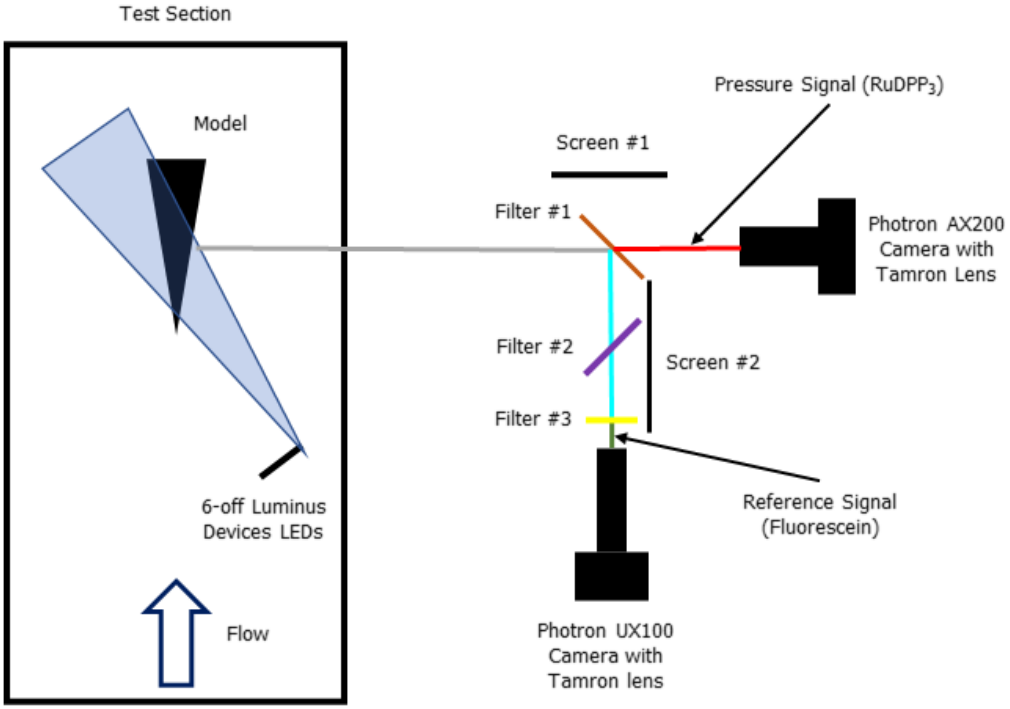

Fig. 5 Schematic diagram of optical layout. Flow is from bottom to top in the test section.

The pressure and reference signals were recorded using two high-speed Photron Fastcam cameras, a Mini-AX200 and a Mini-UX100, respectively. Each camera was fitted with a Tamron 24-70mm f2.8 Di VC USD SP Lens. Black screens were used to help block stray light or reflections. Each camera was operated at 6,400 fps with resolution 1024 x 768 and records the data with 12-bit dynamic range (monochrome). One complication with the use of two different model cameras was the different sensor

sizes: the AX200 has 20 µm pixels and a maximum resolution of 1024 x 1024, whereas the UX100 has 10 µm pixels and a maximum resolution of 1280 x 1024. This difference was accounted for via. each Tamron zoom lens. The alignment error is estimated to be 37 pixels with a scaling difference of 1.1 between the two cameras, indicating the practical difficulty of using a two-camera set up with non-identical sensors.

3.5. Pressure Sensitive Paint

Two formulations of PSP were applied to the conical free-flight model, the details of which are given in Table 3. The main frustum was painted with a white basecoat before 7 cross-coats of solution *j* were applied. In comparison, the aluminium nose piece was anodised and sprayed with 6 cross-coats of solution *m*. For both components the paint was applied using an Anest Iwata LPH-80 air gun fitted with a 0.8 mm nozzle and operated at 20 psig. The black optical tracking markers were painted directly onto the white base coat and protected with masking tape prior to application of the PSP. Fig. 6 shows the coated model after spraying and Fig. 7 shows the model mounted in the HDT test section prior to the first test.

Table 3. PSP Formulations applied to the Free-Flight Cone Model

Solution:		(1)			(2)				Luminophore Concentration			
No:	Type:	$RuDPP_3$ (X mg)	Fluorescein (Y mg)	DCM (ml)	RTV-118 (mg)	TiO_2 (g)	Toluene (ml)		Ru:F (1:x)	[Fluores] [mM]	[$RuDpp_3$] [mM]	[Ru + F] [mM]
j (cone)	PC-PSP	37.41	15.95	24	1200	6.8	56		1.5	0.6	0.4	1.0
m (tip)	AA-PSP	7.02	3.99	30	N/A	N/A	N/A		1.3	0.4	0.2	0.7

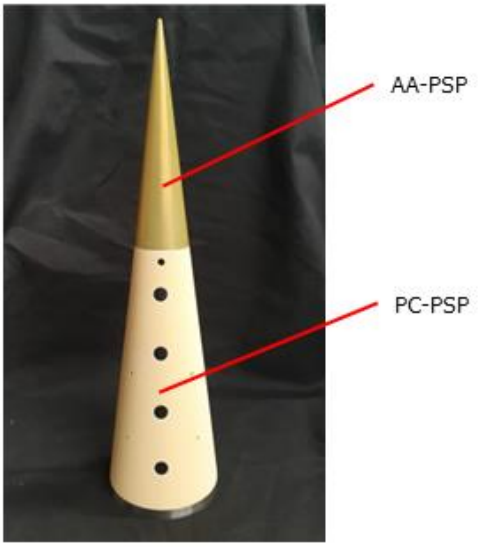

Fig. 6 PSP coated model ready for installation into the test section.

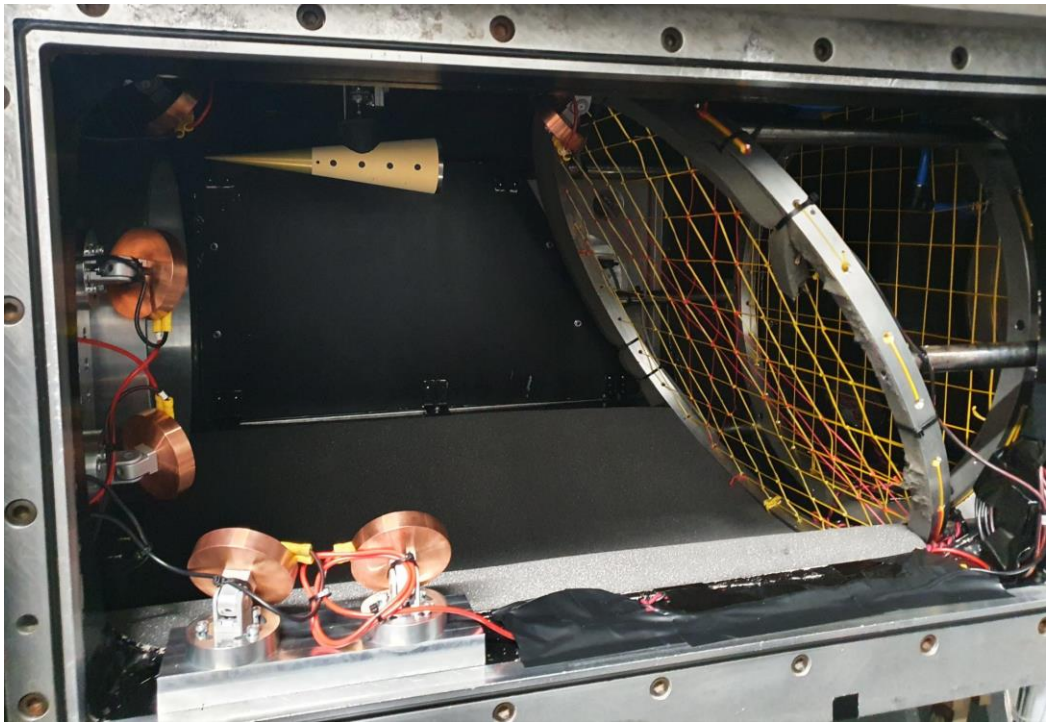

Fig. 7 PSP-coated free-flight cone model mounted in the HDT test section prior to a test.

3.6. Data Reduction

The image processing used in this work for both the wind tunnel experiment and in-situ calibration consisted of four major steps:

1) Optical Tracking
2) Cropping and Scaling
3) Calculation of the Ratio-of-Ratios
4) Application or Calculation of the Calibration Curve

Each of these steps are described as follows.

Optical Tracking

Optical tracking was used to determine the model location within each frame and thereby the displacement of the model during a test. The methodology used was identical to that described in Hyslop et al. [24] so is only briefly described here. The method relies on tracking two of the four black circles painted on the side of the model. Although only two circles are needed, typically four circles are painted on this experimental model to provide redundancy in the event of low image contrast. The algorithm to determine the center point of each circle for every video frame was as follows:

1) Apply Gaussian filter to image and subtract from original (high-pass filter).
2) Apply Canny filter to image so that only pixels detected as an edge are shown [25].
3) Apply Hough transform to find circles in the image after narrowing the search radius [26].
4) Detect pixels in the proximity of the circle located by the Hough transform.
5) Use subpixel detection on the original image at the location where pixels were detected. Subpixel methodology is set out in von Gioi and Randall [27].
6) Fit a circle to the pixels using linear regression, as set out in Laurence and Hornung [5], and use this equation to find the center point of the circle.

The model center of gravity was characterised prior to testing and its position known relative to the circle locations. Angle of attack was determined by detecting the edge of the cone model (following

steps 1-2 used for detecting circles) and fitting a straight line through the detected pixels. Thus, the center of gravity and angle of attack could be inferred for each frame, resulting in the displacement and angle-of-attack history of the model during a test. The image scale was also determined using the known distance between the circles. This scale was found to be 0.737 mm/pixel for the pressure signal and 0.792 mm/pixel for the reference signal. Fig. 8 presents a composite image of the optical tracking data extracted from the pressure signal images. The nozzle centerline and core-flow extent are also indicated, showing the model to be near the centerline during the test flow period.

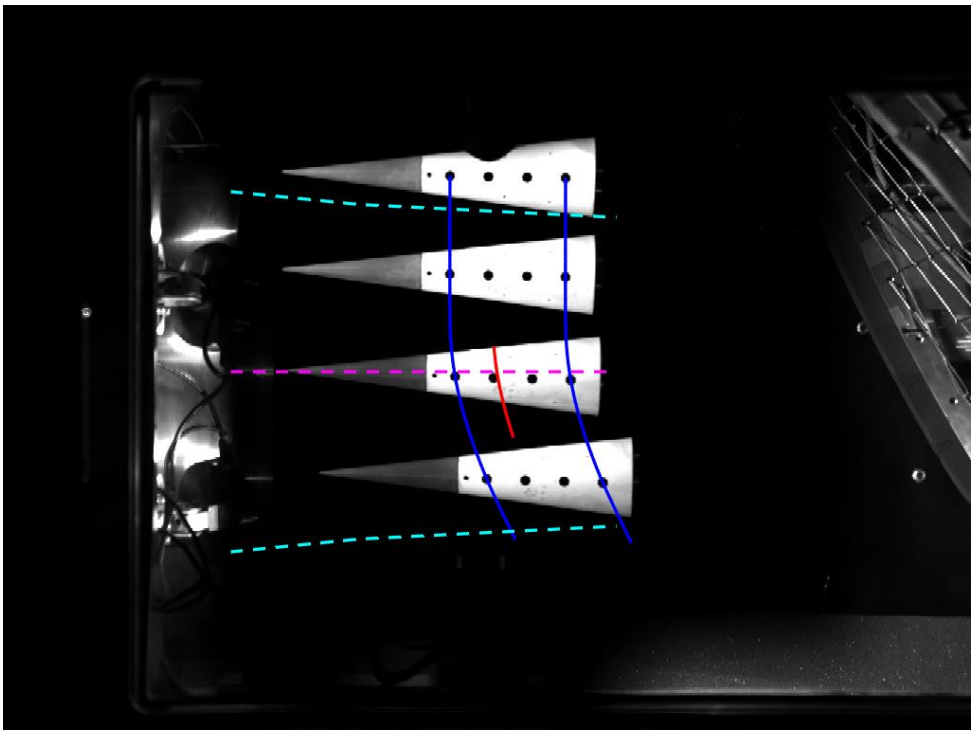

Fig. 8 Composite image of shot 2343 generated from the pressure signal data. Blue solid lines indicate the detected circle centre points; Red solid line indicates the calculated centre of mass location during the test time; Magenta dashed line indicates the facility nozzle centreline; Cyan dashed lines indicate the core-flow extent of the nozzle.

Cropping and Scaling

Following the optical tracking analysis, the known model position was used to crop each frame to a rectangular region around the model, thereby removing unnecessary data. The downstream tracking dot was used as a datum for the cropping process. The final cropped images were typically 367 x 137 pixels. To enable pixel-by-pixel comparison, the differences in scale and resolution of the pressure and reference signals were accounted for by re-sizing the reference signal (measured with the lower resolution UX100 camera) to match the pressure signal. This resizing was achieved using the MATLAB function *imresize* with bicubic interpolation and typically resulted in 7% change in size.

Calculation of Ratio-of-Ratios

Using the cropped and scaled images, the ratio of the pressure and reference intensities are taken on a pixel-by-pixel basis to give $\tilde{I} = I_p/I_r$. This intensity ratio is then combined with the reference condition intensity ratio $(\tilde{I}_R = I_{R,p}/I_{R,r})$ to give the ratio-of-ratios $\tilde{I}_R/\tilde{I}$ as defined in Eq. (2). For the wind tunnel experiments, the reference condition was taken to be ambient temperature and an absolute pressure of 2 kPa with $\tilde{I}_R$ calculated from an in-situ calibration of the model. For the calibration data, I_p and I_p were each calculated as the average of 20 frames recorded with the test section at a steady pressure. The pressure was measured using an Inficon CDG-025D gauge with range 0.7 mbar – 13332 mbar and accuracy 0.2% of the reading.

Application/Calculation of Calibration Curve

In-situ calibration results were fitted with a curve of the form:

$$\frac{\tilde{I}_R}{\tilde{I}} = \frac{K_1 - K_2 p}{K_3 - K_4 p} \tag{5}$$

which is equivalent to Eq. (2) with the reference pressure incorporated into the calibration constants. Two sets of curves were generated – pixel-by-pixel calibrations and single-curve calibrations, in which a small area of the model was averaged and used for the curve fit. A single-curve calibration was generated for each paint used on the model. Using the known calibration constants, Eq. (5) was used to process the wind tunnel data and infer the surface pressure.

4. Results and Discussion

4.1. In-situ Calibration

In-situ calibration was performed before and after the wind tunnel test. For this calibration the model was held in the test section on the electromagnetic release mechanism and the test section incrementally evacuated from ambient to ~100 Pa. At chosen intervals the pressure was held constant and 20 frames were simultaneously recorded on both the pressure and reference signal cameras. Example results for the pressure and reference signals and ratio-of-ratios are provided in Fig. 9. As expected, large variations in intensity are observed over the cone surface in both the pressure and reference signals. These variations are a consequence of differences in illumination intensity and paint uniformity/thickness. In comparison, the ratio-of-ratios presented in Fig. 9c shows significantly less variation, with differences being in the range ±5% over the aluminium cone nose piece (AA-PSP) and ±15% over the cone frustum.

Comparison of the pressure signal contour (Fig. 9a) with the reference signal contour (Fig. 9b) shows a large disparity between the signal levels. The pressure signal over most of the frustum (PC-PSP) is nearly saturating the camera sensor whereas the reference signal is very weak over the entirety of the model. This large difference in SNR for the two signals is a consequence of both inherent differences in the behavior of each luminophore, and the use of an additional optical filter in the reference signal path which comparatively reduces the intensity (cf. Fig. 1 and Fig. 5).

Two black squares are indicated on each image in Fig. 9; one on the nose tip and a second on the rear frustum. These squares indicate the regions used to generate "single-curve" calibrations for each type of paint, the results of which are presented in Fig. 10 for both the pre- and post-test calibrations. Comparing the curves for the different paints, the response of the AA-PSP on the model nose is stronger than that of the PC-PSP on the frustum for both the pre- and post-test calibrations. This is expected because the anodised aluminium is more porous than polymer-ceramic and so deactivates more readily in the presence of oxygen. Additionally, comparison of the pre- and post-test calibration data indicates that the AA-PSP is significantly more robust than the PC-PSP – there is little change in the calibration curve for AA-PSP while a significant change occurred for the PC-PSP. The improved robustness of the AA-PSP over the PC-PSP was also observed during handling of the model. It is unclear whether the degradation of the PC-PSP occurred due to the flow or was primary a consequence of the model hitting the foam base of the test section at the end of the free-flight.

Of particular concern with the results in Fig. 10 is the large degree of scatter in the data points, particularly at low pressures (<5 kPa). The reasons for this scatter require further investigation. It is interesting to note that for the AA-PSP the scatter is comparatively lower for the post-test calibration than for the pre-test calibration. The offset of the calibration curves with respect to the calibration points is a consequence of data points recorded at higher pressures (up to ambient). It is anticipated that curve-fitting over a smaller pressure range will decrease this offset.

The quality of calibrations (both per-pixel and "single-curve") were assessed by re-applying the calibration curve to a measured ratio-of-ratios and examining how well the quiescent pressure was recovered. Results are given in Fig. 11 as the percentage difference relative to the known pressure 3 kPa. On the nose piece (AA-PSP), the pressure is well recovered independent of whether a "single-curve" or per-pixel calibration is used. Such a result was expected given the uniformity of the ratio-of-ratios observed in the calibration data for this region (cf. Fig. 9c). Surprisingly, a similar consistency was not observed for the frustum (PC-PSP). On this component the per-pixel calibration performed significantly worse than the "single-curve" calibration, counter to expectations. The exact cause for this result is currently unknown and requires further investigation. Our current hypothesis is that it is related

to near saturation of the pressure signal camera over the central region of the frustum at low calibration pressures.

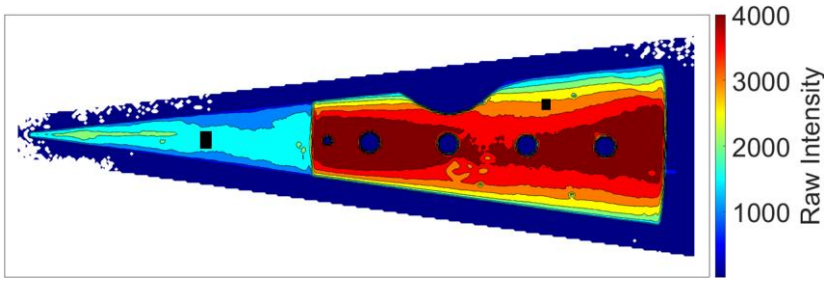

(a) Pressure signal intensity contour

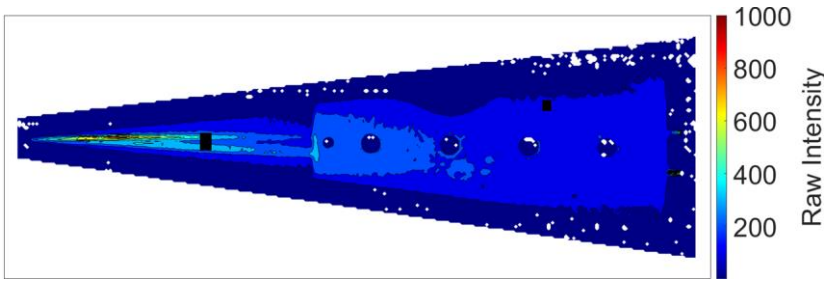

(b) Reference signal intensity contour

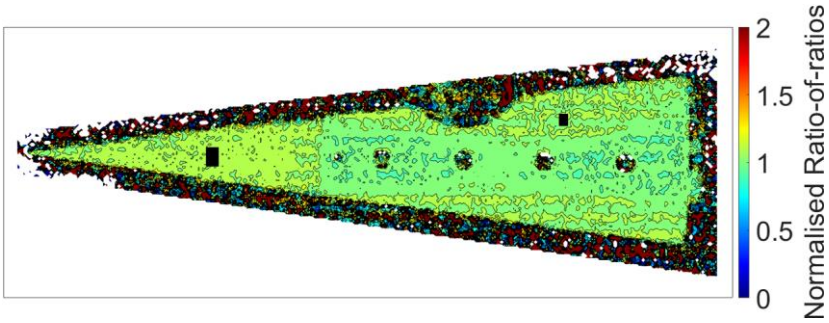

(c) Ratio-of-ratios contour

Fig. 9 Example in-situ calibration results at p = 3 kPa (pre-shot 2343). The pressure and reference signal plots each represent the average of 20 frames.

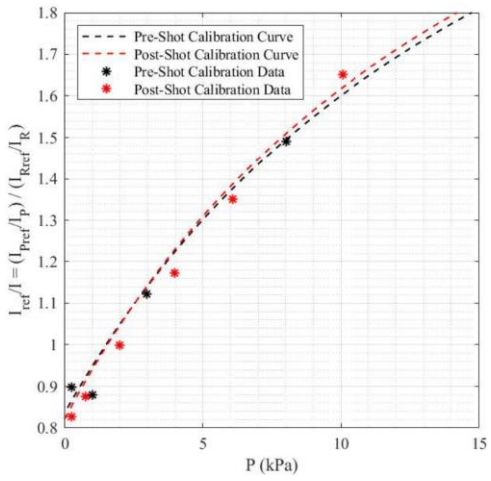

(a) AA-PSP calibration curve; model nose piece

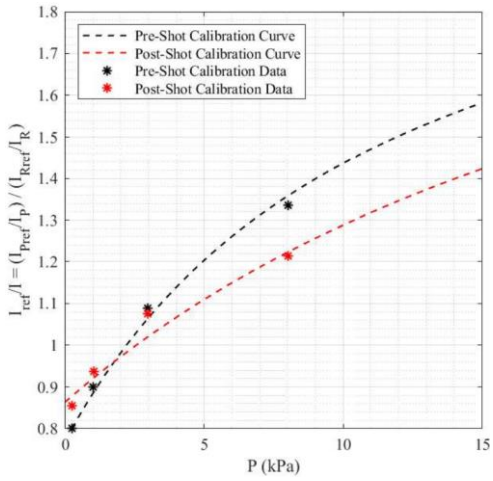

(b) PC-PSP calibration curves; model frustum

Fig. 10 Comparison of pre- and post- test in-situ calibration results for the single-curve calibrations.

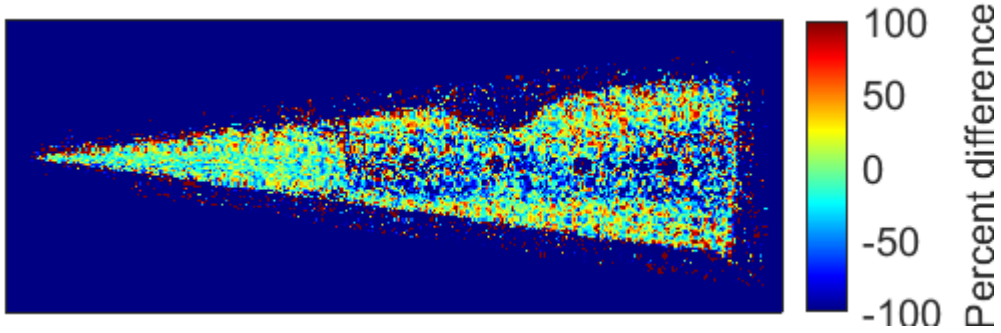

(a) Pixel-by-pixel calibration

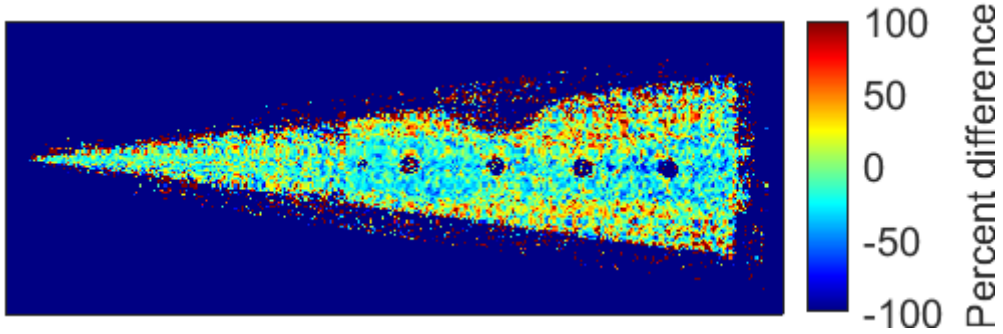

(b) "Single-curve" calibration

Fig. 11 Error in recovered calibration pressure for p = 3 kPa.

4.2. HDT Test

A single free-flight experiment is presented here for the PSP-coated conical model. Fig. 12 presents the calculated surface pressure using the "single-curve" calibration for two instances during the experiment, immediately after release of the model, before flow arrival (Fig. 12a) and during the middle of the steady test-flow period (Fig. 12b). Consider Fig. 12a – the model has only just been released and is beginning to accelerate under gravity into the quiescent test section gas which is at a pressure of approximately 100 Pa. In contrast, the PSP results indicate pressures in the approximate range 0.5 to 4.5 kPa, an order of magnitude greater. Significantly non-uniformity also exist which were not present in the calibration results (cf. Fig. 11b), despite the model being in practically the same location within the test section and theoretically under equivalent illumination. Our current hypothesis is that this related to the low SNR of the reference signal and imbalance in signal strength between the pressure and reference signals.

The pressure distribution during the middle of the steady test flow period is given in Fig. 12b. Similar to Fig. 12a, significant non-uniformities are present on the aluminium nose piece with the entire upper half measuring >15 kPa, a non-physical result. The frustum of the cone also features non-uniformities, although pressures are typically in the range 0 – 10 kPa and large sections are in the range 0 – 5 kPa.

A comparison of the PSP result with numerical predictions is provided in Fig. 13 for the centreline ray of the model. For the PSP result, regions coinciding with the optical tracking dots have been set to 0 kPa. Three numerical results are provided: a computational fluid dynamics (CFD) result for 0° angle-of-attack (AoA), a panel-method result for 0° AoA and a panel-method result for 1.4° AoA. The CFD result was generated using the open-source compressible flow solver *Eilmer* [28] assuming laminar viscosity with a no-slip, isothermal wall-boundary condition at 300 K and using a thermally perfect single-species air model. The Newton-Krylov update scheme was used to accelerate convergence to steady state and the wall y+ was less than one everywhere. The panel-method results were generated using the code developed by Hyslop et al [10] assuming calorically perfect air.

The transition between the AA-PSP on the nose tip and PC-PSP on the frustum occurs at x/L = 0.43. On the frustum the PSP indicates a pressure < 5 kPa, which is somewhat comparable with the expected

pressure of 1.8 kPa. It is interesting that the comparison between the PSP and numerical results improves towards the rear of the model. Noting that the most downstream optical tracking dot was used as a datum for the PSP processing, this suggests that some differences in alignment and scaling exist between the four images used in the ratio-of-ratios calculation. Based on the measured lift coefficient, the model was at 1.4° AoA during the test time. The corresponding windward and leeward ray pressure distributions are presented in Fig. 13 but do not significantly improve the comparison with, nor bound, the experimental result. Matching the PSP pressure levels requires an angle-of-attack of 7° which was not the case for this experiment. Thus, further investigations and re-analysis of the PSP calibration and shot data are required to isolate the cause of the discrepancies.

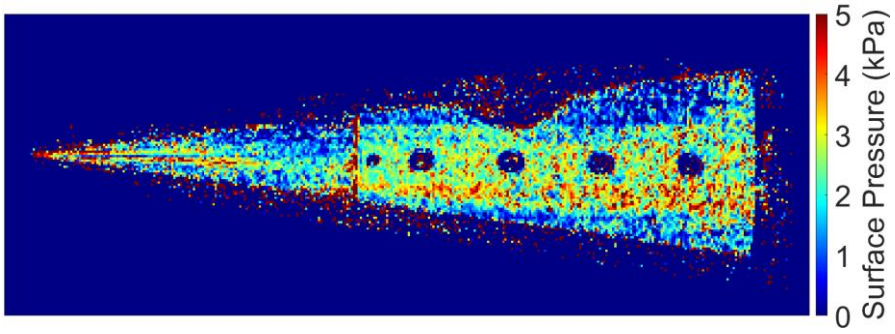

(a) Immediately post-release of the model, pre-flow arrival (frame 520)

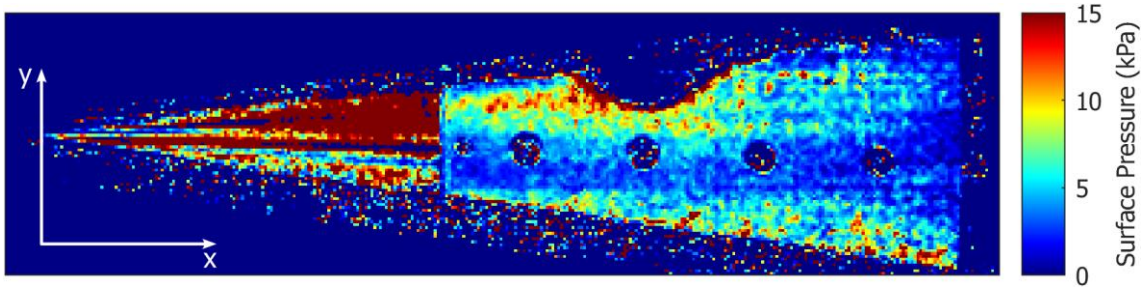

(b) During steady test flow period (frame 1779)

Fig. 12 Cone surface pressures for two instances in time from the free-flight experiment (shot 2343)

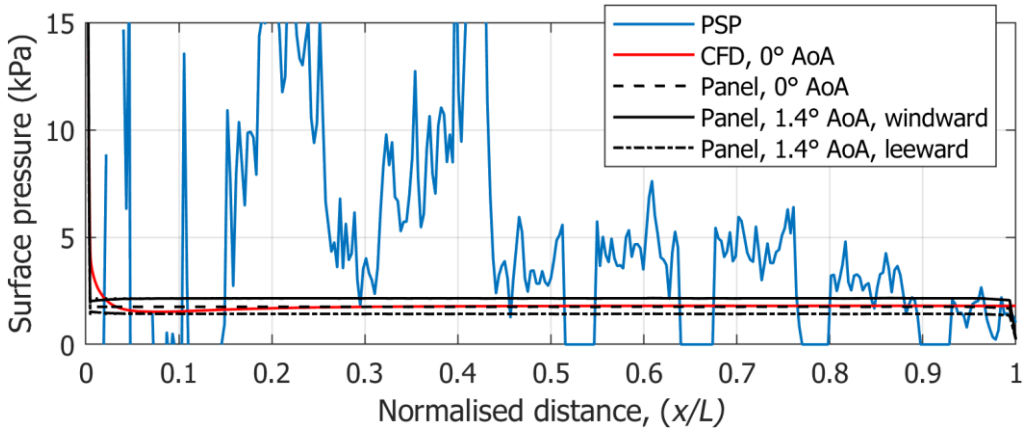

Fig. 13 Comparison of PSP and Numerical pressure distributions along the cone mid-line. Regions coinciding with the optical tracking dots have been manually set to 0.

5. Conclusion

This paper has presented our first attempt at utilising two-colour PSP for the measurement of surface pressure on a free-flying aerodynamic model in the Oxford High Density Tunnel at a Mach 7 test condition. The model consisted of a 7° half-angle cone with 1.25mm radius blunt nose tip and was 250 mm in length. It featured an on-board data acquisition system for the measurement of 6-components of force/moment. Two different formulations of binary-PSP were applied to the model, each using RuDDP3 as the pressure sensors and Luminophore as the reference sensor; the nose piece was coated with AA-PSP and the frustum with PC-PSP. These two formulations were selected from fourteen mixtures evaluated using a benchtop calibration rig for pressure and temperature sensitivity, and overall robustness. During the experiment the model was optically tracked via two high speed cameras which enabled the PSP output to be analysed via. the ratio-of-ratios method. Difficulty in ensuring consistent alignment between the four images needed for the data reduction, limited the results to just a single frame of the high-speed video. The experimentally measured pressure distribution showed significant non-physical non-uniformities and was at best double the expected pressure based on numerical and analytical predictions. Despite the difficulties the results of this work are promising and show that further improvements in data processing and calibration are needed for binary-PSP to be useful in free-flight experiments in the Oxford High Density Tunnel.

Acknowledgements

The authors wish to thank Andreea Dabija for preparing the PSP mixtures and spraying the calibration coupons and experimental model, and Raghul Ravichandran for running the Eilmer simulation of the model.

References

[1] R. Wuilbercq, F. Pescetelli, E. Minisci and R. E. Brown, "Influence of Boundary Layer Transition on the Trajectory Optimisation of a Reusable Launch Vehicle," in *19th AIAA Internation Space Planes and Hypersonic Systems and Technologies Conference*, Atlanta, GA, 2014, DOI: 10.2514/6.2014-2362.

[2] L. Bernstein and R. C. Pankhurst, "Force Measurements in Short-Duration Hypersonic Facilities," North Atlantic Treaty Organization, Advisory Group for Aerospace Research and Development, AGARDograph No. 214, 1975.

[3] D. J. Mee, W. J. Daniel and J. M. Simmons, "Three-component force balance for flows of millisecond duration," *AIAA Journal,* vol. 34, no. 3, pp. 590 - 595, 1996, DOI: 10.2514/3.13108.

[4] L. J. Doherty, M. K. Smart and D. J. Mee, "Measurement of Three-Components of Force on an Airframe Integrated Scramjet at Mach 10," in *20th AIAA International Space Planes and Hypersonic Systems and Technologies Conference*, Glasgow, Scotland, 2015, DOI: 10.2514/6.2015-3523.

[5] S. J. Laurence and H. G. Hornung, "Image-Based Force and Moment Measurement in Hypersonic Facilities," *Experiments in Fluids,* vol. 46, no. 2, pp. 343 - 353, 2009, DOI: 10.1007/s00348-008-0565-6.

[6] A. K. Owen and F. K. Owen, "Hypersonic Free Flight Measurement Techniques," in *22nd International Congress on Instrumentation in Aerospace Simulation Facilities*, 2007, DOI: 10.1109/ICIASF.2007.4380898.

[7] G. S. Pick, "Sting Effects in Hypersonic Base Pressure Measurements," Naval Ship Research and Development Center, Bethesda, Maryland, USA, 1971, URL: https://apps.dtic.mil/sti/citations/AD0741888.

[8] H. Tanno, K. Sato, T. Komuro, K. Itoh and M. Takahashi, "Aerodynamic characteristics of generic models under real-gas conditions in the free-piston shock tunnel HIEST," in *15th AIAA International Space Planes and Hypersonics Systems and Technologies Conference*, Dayton, Ohio, 2008, DOI: 10.2514/6.2008-2567.

[9] C. Kennell, A. J. Neely, D. R. Buttsworth, R. Choudhury and M. Tahtali, "Free Flight Testing in Hypersonic Flows: HEXAFLY-INT EFTV," in *54th AIAA Aerospace Sciences Meeting*, San Diego, California, USA, 2016, DOI: 10.2514/6.2016-1152.

[10] A. Hyslop, L. J. Doherty and M. McGilvray, "Free-Flight Aerodynamic Testing of a 7 Degree Half-Angle Cone," in *AIAA SciTech, AIAA-2022-1324*, San Diego, 2022, DOI: 10.2514/6.2022-1324.

[11] Luminus Devices, Inc., "PT-120-TE Product Datasheet," [Online]. Available: https://download.luminus.com/datasheets/Luminus_PT-120_Datasheet.pdf. [Accessed April 2019].

[12] A. Bioquest, "Spectrum [Fluorescein]," [Online]. Available: https://www.aatbio.com/fluorescence-excitation-emission-spectrum-graph-viewer/Fluorescein. [Accessed April 2020].

[13] M. K. Quinn, L. Yang and K. Kontis, "Pressure-Sensitive Paint: Effect of Substrate," *Sensors,* vol. 11, no. 12, pp. 11649 - 11663, 2011, DOI: 10.3390/s111211649.

[14] J. W. Gregory, H. Sakaue, T. Liu and J. P. Sullivan, "Fast Pressure-Sensitive Paint for Flow and Acoustic Diagnostics," *Annual Review of Fluid Mechanics,* vol. 46, pp. 303 - 330, 2014, DOI: 10.1146/annurev-fluid-010313-141304.

[15] D. Peng and Y. Liu, "Fast pressure-sensitive paint for understanding complex flows: from regular to harsh environments," *Experiments in Fluids,* vol. 61, no. 8, 2020, DOI: 10.1007/s00348-019-2839-6.

[16] J. Vieira, "Thermal and Aerodynamic Investigation of Innovative Cooling Designs of Blade Tips," DPhil Thesis (submitted). Oxford Thermofluids Institute, University of Oxford., 2022.

[17] Y. Egami, A. Hasegawa, Y. Matsuda, T. Ikami and H. Nagai, "Ruthenium-based fast-responding pressure-sensitive paint for measuring small pressure fluctuation in low-speed flow field," *Measurement Science and Technology,* vol. 32, no. 2, p. 024003, 2020, DOI: 10.1088/1361-6501/abb916.

[18] T. Liu, J. Sullivan, K. Asai, C. Klein and Y. Egami, Pressure and Temperature Sensitive Paints, 2nd ed., Springer Nature, 2021.

[19] M. McGilvray, L. J. Doherty, A. J. Neely, R. Pearce and P. T. Ireland, "The Oxford High Density Tunnel," in *20th AIAA International Space Planes and Hypersonic Systems and Technologies Conference*, Glasgow, Scotland, 2015, DOI: 10.2514/6.2015-3548.

[20] S. Wylie, L. J. Doherty and M. McGilvray, "Commissioning of hte Oxford High Density Tunnel for Boundary Layer Stability Measurements at Mach 7," in *48th AIAA Fluid Dynamics Conference*, Atlanta, Georgia, 2018, DOI: 10.2514/6.2018-3074.

[21] A. Widodo and D. Buttsworth, "Stagnation Temperature in a Cold Hypersonic Flow Produced by a Light Free Piston Compression Facility," *Experiments in Fluids,* vol. 54, no. 1486, 2013, DOI: 10.1007/s00348-013-1486-6.

[22] T. Hermann, M. McGilvray, C. Hambidge, L. J. Doherty and D. Buttsworth, "Total Temperature Measurements in the Oxford High Density Tunnel," in *International Conference on Flight Vehicles, Aerothermodynamics and Re-entry Missions & Engineering (FAR)*, Manopoli, Italy, 2019.

[23] L. P. McQuellin, C. M. Kennell, A. J. Neely, M. J. Sytsma, T. Silvester, R. Choudhury and D. R. Buttsworth, "Investigating endo-atmospheric separation of a hypersonic flyer-sustainer using wind tunnel based free-flight," in *23rd AIAA International Space Planes and Hypersonic Systems and Technologies Conference*, 2020, DOI: 10.2514/6.2020-2451.

[24] A. Hyslop, L. J. Doherty, M. McGilvray, A. Neely, L. P. McQuellin, J. Barth and G. Mullen, "Free-Flight Aerodynamic Testing of the Skylon Space Plane," *Journal of Spacecraft and Rockets,* vol. 58, no. 5, 2021, DOI: 10.2514/1.A34937.

[25] J. Canny, "A Computation Approach to Edge Detection," *IEEE Transactions on Pattern Analysis and Machine Intelligence,* Vols. PAMI-8, no. 6, pp. 679 - 698, 1986, DOI: 10.1109/TPAMI.1986.4767851.

[26] P. V. C. Hough, "Method and Means for Recognizing Complex Patterns". USA Patent 30696541962, Dec 1962.

[27] R. G. von Gioi and G. Randall, "A Sub-Pixel Edge Detector: An Implementation of the Canny/Devernay Algorithm," *IPOL Journal,* vol. 7, pp. 347 - 372, Nov. 2017, DOI: 10.5201/ipol.2017.216.

[28] N. N. Gibbons, K. A. Damm, P. A. Jacobs and P. J. Gollan, "Eilmer: an Open-Source Multi-Physics Hypersonic Flow Solver," *arXiv,* 2022, DOI: 10.48550/arXiv.2206.01386.